CWP-113P
January 1992

3-D migration to zero offset for a constant velocity gradient: an analytical formulation

Michel Dietrich* and Jack K. Cohen‡

Appeared in *Geophysical Prospecting*, **41**, July 1993, pp 621-643.

* IRIGM, BP 53X, 38041 Grenoble Cedex, France, and Center for Wave Phenomena, Colorado School of Mines, Golden, CO 80401, USA.

‡ Center for Wave Phenomena, Colorado School of Mines, Golden, CO 80401, USA.

ABSTRACT

Migration to zero offset (MZO) is a prestack partial migration process that transforms finite offset seismic data into close approximation to zero offset data, regardless of the reflector dips that are present in the data. MZO is an important step in the standard processing sequence of seismic data, but is usually restricted to constant velocity media. Thus, most MZO algorithms are unable to correct for the reflection point dispersal caused by ray bending in inhomogeneous media.

We present an analytical formulation of the MZO operator for the simplest possible variation of velocity within the earth − a constant gradient in the vertical direction. The derivation of the MZO operator is carried out in two steps. We first derive the equation of the constant traveltime surface for linear $V(z)$ velocity functions and show that the isochron can be represented by a fourth-degree polynomial in x, y and z. This surface reduces to the well-known ellipsoid in the constant-velocity case, and to the spherical wavefront obtained by Slotnick in the coincident source-receiver case.

We then derive the kinematic and dynamic zero offset corrections in parametric form by using the equation of the isochron. The weighting factors are obtained in the high frequency limit by means of a simple geometrical spreading correction. Our analytical results show that the MZO operator is a multivalued, saddle-shaped, operator with marked dip moveout effects in the crossline direction. However, the amplitude analysis and the distribution of dips along the MZO impulse response show that the most important contributions of the MZO operator are concentrated in a narrow zone along the inline direction. In practice, MZO processing requires approximately the same trace spacing in the inline and crossline directions to avoid spatial aliasing effects.

INTRODUCTION

The concept of equal reflection time surfaces, −or aplanatic surfaces, by analogy with optics− has been extensively used in early seismic imaging techniques, mainly for the dip migration of *post-stack* seismic data (Hagedoorn, 1954). Isochronous surfaces have regained interest in recent years with the development of dip moveout (DMO) processing of *pre-stack* seismic data, an operation also referred to as a migration to zero offset (MZO) (Deregowski and Rocca, 1981; Perkins and French, 1990).

The shape of the constant traveltime surfaces can be computed numerically for arbitrarily complex velocity models (Musgrave, 1961), but can also be derived analytically in some simple situations. The constant velocity case is trivial, and corresponds to the well-known ellipsoid whose foci coincide with the source and receiver locations. Heterogeneous media are more difficult to handle because of the complexity of the ray geometry. There are, however, several exceptions to this rule: the rays are circular when the velocity is a linear function of the spatial coordinates, parabolic if the slowness-squared varies linearly within the medium, and follow sinusoidal trajectories in a quadratic slowness profile (see, e.g., Wunsch, 1987). As the simplest possible variation of velocity, the case of a constant velocity gradient has drawn the attention of the seismic community for many decades. Thus, Slotnick (1936a, 1936b, 1959) showed that the *wavefront* has a simple form when the velocities are linearly increasing (or decreasing) with depth: it is an expanding sphere whose center moves downward (or upward) as a function of time.

In this paper, we extend Slotnick's results to the non-zero offset case and show that the constant traveltime surface for a linear distribution of velocity is given by a quartic equation. The analysis presented in the first part of the paper gives a simple demonstration of this result, and was facilitated by a preliminary study performed with the *Mathematica*™ software (Wolfram, 1988) to obtain the general form of the solution. In addition, the calculations are conducted with the usual approximation that the reflectors can be considered as small and localized perturbations of a relatively simple background velocity field. We will therefore assume that the traveltimes can be accurately computed by tracing circular rays in a one-dimensional medium, although the actual medium is vertically and laterally heterogeneous in terms of reflectivity.

In the second part of the paper, we use the equation of the constant traveltime surface to derive the kinematic and dynamic MZO corrections for a linear velocity gradient. MZO, or its practical implementation as a sequence of normal moveout and dip moveout corrections, is routinely used in the seismic industry to overcome the limitations of the common midpoint stacking technique, or to avoid the high computational costs of a full prestack migration. In fact, most of the success of this approach derives from the simplicity of the dip moveout operator in a constant velocity medium. The zero-offset mapping is then characterized by a perfectly elliptical impulse response that intersects the source and the receiver at zero time. Furthermore, this process does not depend on velocity and can be efficiently implemented using integral (Kirchhoff-like) methods (Deregowski and Rocca, 1981; Hale, 1991), or Fourier transform methods (Hale, 1984; Notfors and Godfrey, 1987). In spite of these advantages, constant-velocity MZO can lead to unacceptable errors in the imaging of steeply dipping reflectors, when the seismic wave

velocity varies rapidly in the subsurface. In such cases, MZO should be improved to handle the velocity variations, at least approximately.

MZO in inhomogeneous media is more complex and computationally expensive than constant-velocity MZO, and has been mainly investigated using numerical techniques. Thus, Artley (1991) showed that the MZO operator for depth-variable velocity differs from the classical dip moveout ellipse by one or several additional branches. Perkins and French (1990) studied the case of a constant velocity gradient and showed that there can be marked dip moveout effects in the crossline direction. They derived a two-dimensional, saddle-shaped operator suitable for 3-D dip moveout processing. 3-D dip moveout for vertically varying media was also discussed by Meinardus and Schleicher (1991), Shang and Starr (1991), and Witte (1991).

The analysis presented here is an exact treatment for a constant velocity gradient. Our derivation of the MZO operator follows the definition of MZO: a process designed to move the seismic energy in a finite offset experiment to where it would have been recorded in an equivalent zero offset experiment. This process includes an amplitude correction which will be approximated by a geometrical spreading correction. Our objective is to describe the general anatomy of the MZO operator for linear $V(z)$ velocity functions and to show that its main characteristics can be expressed analytically. We will not discuss the practical implementation of the MZO processing with real data or the numerical problems that may arise in this implementation. For these reasons, and because MZO is basically a partial migration of seismic data, we will use the general term "MZO" instead of the more specific term "DMO" to characterize the zero offset corrections.

I. THE CONSTANT TRAVELTIME SURFACE

The geometry of the problem is depicted in Figure 1. We consider a cartesian coordinate

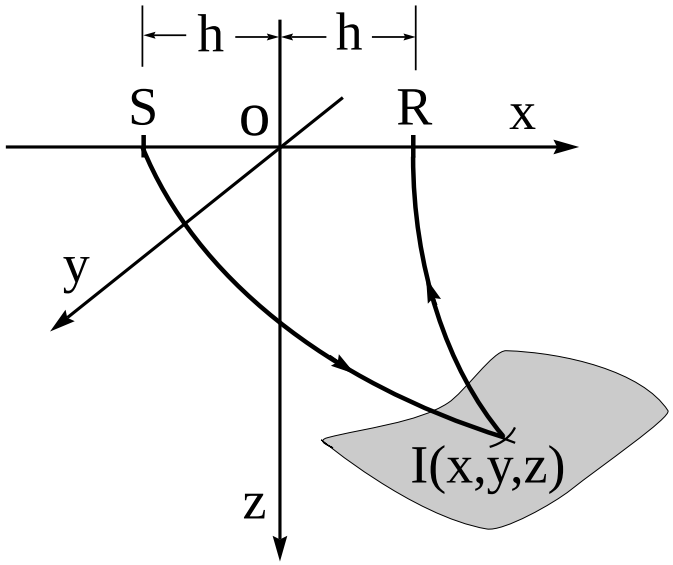

FIG. 1. The constant traveltime problem between a fixed source S, a reflection point I, and a fixed receiver R.

system (x, y, z), and assume that the velocity function has the form

$$V(z) = V_0 + kz \quad , \tag{1}$$

where V_0 is the seismic velocity at the surface. The source S and receiver R are located along the x-axis at points $S(-h, 0, 0)$ and $R(h, 0, 0)$. In the following, we shall refer to the x- and y-axes as the *inline* and *crossline* directions.

The equal reflection time surface is the locus of the reflection points $I(x, y, z)$ such that

$$T = t_{SI} + t_{IR} = \text{constant} \quad . \tag{2}$$

To solve this problem, it is convenient to rewrite equation (1) in the reduced form

$$\hat{z} = \hat{z}_0 + z \quad , \tag{3}$$

where $\hat{z} = V(z)/k$ and $\hat{z}_0 = V_0/k$. The change of variable defined in equation (3) is a simple translation, but has a special meaning. The new variable $\hat{z}$ vanishes at depth $z = -\hat{z}_0$ which is the z-coordinate of the center of all circular rays emitted or received at the surface of the medium. $\hat{z}$ should therefore be considered as the *natural* or *intrinsic* depth variable of our traveltime problem. In practice, the change of variables from z to $\hat{z}$ greatly simplifies the resolution of the equations, and allows us to write the final solution in a compact form. For that reason, most of the calculations presented here are given in the new coordinate system $(x, y, \hat{z})$.

The first (and most important) step in the derivation of the constant traveltime surface is to express the traveltime t as a function of the spatial variables x, y and $\hat{z}$. We show in the Appendix that the traveltime t between the origin O and a given point $I(x,y,z)$ is given by an expression of the form $t = \tau/k$, where the dimensionless variable τ is defined by

$$\tau = \cosh^{-1}\left[\frac{\xi^2 + \hat{z}^2 + \hat{z}_0^2}{2\ \hat{z}\hat{z}_0}\right] \quad , \tag{4}$$

and $\xi = \sqrt{x^2 + y^2}$ is the horizontal distance travelled along the ray.

The constant traveltime condition (2) can then be expressed as

$$\tau_{SI} + \tau_{IR} = kT \quad ,$$

or

$$\cosh\ (\tau_{SI} + \tau_{IR}) = \cosh kT \tag{5}$$

to exploit the particular form of the traveltime function. In the above expressions, τ_{SI} and τ_{IR} are given by equation (4), with ξ replaced by

$$\xi_{SI} = \sqrt{(x+h)^2 + y^2} \qquad \text{and} \qquad \xi_{IR} = \sqrt{(x-h)^2 + y^2} \quad ,$$

respectively, and h is half-offset between source and receiver, as depicted in Figure 1.

The expansion of equation (5) leads to the relationship

$$2\cosh kT \cosh\tau_{SI} \cosh\tau_{IR} - (\cosh^2\tau_{SI} + \cosh^2\tau_{IR}) = \sinh^2 kT \quad , \tag{6}$$

in which

$$\begin{aligned} \cosh\tau_{SI}\cosh\tau_{IR} &= \left[\frac{\xi_{SI}^2 + \hat{z}^2 + \hat{z}_0^2}{2\ \hat{z}\hat{z}_0}\right]\left[\frac{\xi_{IR}^2 + \hat{z}^2 + \hat{z}_0^2}{2\ \hat{z}\hat{z}_0}\right] \\ &= \frac{\Gamma^2 - 4\ x^2h^2}{4\ \hat{z}^2\hat{z}_0^2} \quad , \end{aligned} \tag{7}$$

$$\begin{aligned} \cosh^2\tau_{SI} + \cosh^2\tau_{IR} &= \left[\frac{\xi_{SI}^2 + \hat{z}^2 + \hat{z}_0^2}{2\ \hat{z}\hat{z}_0}\right]^2 + \left[\frac{\xi_{IR}^2 + \hat{z}^2 + \hat{z}_0^2}{2\ \hat{z}\hat{z}_0}\right]^2 \\ &= \frac{\Gamma^2 + 4\ x^2h^2}{2\ \hat{z}^2\hat{z}_0^2} \quad , \end{aligned} \tag{8}$$

$$\text{with} \qquad \Gamma = x^2 + y^2 + \hat{z}^2 + \hat{z}_0^2 + h^2 \quad .$$

The equation of the constant traveltime surface is finally obtained by substituting expressions (7) and (8) into equation (6), which gives

$$\Gamma^2 \ - \ 4\ x^2h^2\frac{\cosh kT + 1}{\cosh kT - 1} \ - \ 2\ \hat{z}^2\hat{z}_0^2\frac{\sinh^2 kT}{\cosh kT - 1} \ = \ 0 \quad ,$$

that is,

$$\begin{aligned} F(x,y,z,T) \ \equiv \ & [\ x^2 + y^2 + \hat{z}^2 + \hat{z}_0^2 + h^2\ ]^2 \\ & - \ 4\ x^2h^2\coth^2(kT/2) \ - \ 4\ \hat{z}^2\hat{z}_0^2\cosh^2(kT/2) \ = \ 0 \quad . \end{aligned} \tag{9}$$

The expression obtained is a relatively simple fourth-degree polynomial which is symmetric in x, y and $\hat{z}$. However, the complete expansion of this polynomial in terms of the original variables x, y and z contains 14 terms, and includes all even and odd powers of z up to the fourth degree. Equation (9) also shows that x and $\hat{z}$ are solutions of a quartic equation, whereas y is solution of a second-degree equation. It may therefore be anticipated that the isochron has a simpler shape in the crossline direction than in the inline direction.

The isochronous surface defined above admits a number of particular cases and shows some interesting properties. Thus, in a homogeneous medium $V(z) \equiv V_0$, it can be demonstrated that the isochron reduces to the familiar ellipsoid

$$\frac{x^2}{(V_0 T/2)^2} + \frac{y^2}{(V_0 T/2)^2 - h^2} + \frac{z^2}{(V_0 T/2)^2 - h^2} = 1 \quad . \tag{10}$$

In the coincident source-receiver case $h = 0$, equation (9) degenerates to the second-degree polynomial

$$x^2 + y^2 + \{\ z - \hat{z}_0\ [\ \cosh(kT/2) - 1\ ]\ \}^2 = \hat{z}_0^2\ \sinh^2(kT/2) \tag{11}$$

derived by Slotnick (1959): the isochron is a sphere whose center lies on the z-axis at depth $\hat{z}_0\ [\ \cosh(kT/2) - 1\ ]$, and whose radius is $\hat{z}_0\ \sinh(kT/2)$.

Similarly, when $x = 0$, equation (9) becomes

$$y^2 + \{\ z - \hat{z}_0\ [\ \cosh(kT/2) - 1\ ]\ \}^2 = \hat{z}_0^2\ \sinh^2(kT/2) - h^2 \quad . \tag{12}$$

Consequently, the cross-section of the constant traveltime surface in the $y - z$ plane is a circle centered at point $(0, \hat{z}_0\ [\ \cosh(kT/2) - 1\ ])$, with a radius equal to $\sqrt{\hat{z}_0^2\ \sinh^2(kT/2) - h^2}$. This result has an interesting generalization which was first pointed out by Resnick (1990): the intersection of the constant traveltime surface $F(x, y, z, T) = 0$ with *any* oblique plane $x = \hat{z} \tan\phi$ parallel to the y-axis and passing through the point $(0, 0, -\hat{z}_0)$ is a circle, in terms of the coordinate y and of the "slant" variable $\hat{z}' = \hat{z}/\cos\phi$. The constant traveltime surface may therefore be considered as a collection of circular slices defined by the angle ϕ.

Figures 2 and 3 display the shape of the constant traveltime surface for a fixed traveltime T, and for four different values of the half source-receiver offset h. Figure 2 shows the isochronous surface in both the positive and negative z domains, and gives a complete graphical solution to the constant traveltime problem. Indeed, it should be noted that the negative part ($z < 0$) of the isochronous surface corresponding to a positive gradient k is nothing else than the positive part ($z > 0$) of the isochron corresponding to the negative gradient $-k$. Therefore, the representation of the entire surface allows us to describe these two situations at the same time. Figure 3 depicts the trace of the isochron at the surface of the ground.

For zero-offset (Figures 2a and 3a), the constant traveltime surface is the sphere represented by equation (11), and a circle in the horizontal plane $z = 0$. This case differs from that of constant velocity by the fact that the sphere is shifted downward, therefore allowing the dip angle of the reflectors to exceed 90 degrees near the surface.

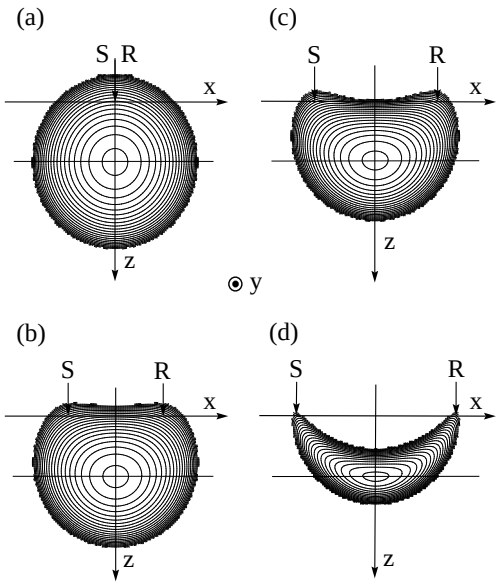

FIG. 2. Graphical representation of the constant traveltime surface for a fixed traveltime T, and for four different values of the half source-receiver offset h. The contour levels represent the y dimension of the surface. In this example, $V_0 = 2$ km/s, $k = 1$ /s, and $T = 3.4$ s. (a) $h = 0$; (b) $h = 3$; (c) $h = 3.8$; and (d) $h = 5$ km.

As h is increased from 0 to 3 km (Figures 2b and 3b), the upper part of the sphere is progressively flattened in the z-direction and stretched along the x-axis. However, the isochron can be characterized by two invariant parameters: the x-coordinate of the vertical tangent in the $y = 0$ plane, and the z-coordinate of the vertical tangent in the $x = 0$ plane are independent of the source-receiver offset. These two factors are respectively associated with the maximum horizontal extent of the surface, and with the depth of the "center" of the surface (see equation 12). The analytical expressions for these parameters are given in Table 1, along with the coordinates of some other particular points of the constant traveltime surface.

Figure 2b also shows that the reflections at 90 degrees (on vertical reflectors) occur at a shallower depth in the inline direction than in the crossline direction. As h increases, these reflections progressively move toward the surface in the inline plane, but remain at a constant depth in the crossline plane.

	Principal (Lower) Surface		**Upper Surface**	
	x **direction**	y **direction**	x **direction**	y **direction**
Reflections at the surface	$x = \pm[(C_T - 1)/S_T]\sqrt{2\hat{z}_0^2(C_T + 1) + h^2}$ $y = 0$ $z = 0$	$x = 0$ $y = \pm\sqrt{2\hat{z}_0^2(C_T - 1) - h^2}$ $z = 0$	$x = \pm[(C_T + 1)/S_T]\sqrt{h^2 - 2\hat{z}_0^2(C_T - 1)}$ $y = 0$ $z = 0$	– – –
Vertical reflectors ($\pm$ 90 deg.)	$\boxed{x = \pm\hat{z}_0 S_T}$ $y = 0$ $z = -\hat{z}_0 + \sqrt{\hat{z}_0^2 {C_T}^2 - h^2}$	$x = 0$ $y = \pm\sqrt{\hat{z}_0^2 {S_T}^2 - h^2}$ $\boxed{z = \hat{z}_0(C_T - 1)}$	– – –	$x = 0$ $y = \pm\sqrt{\hat{z}_0^2 {S_T}^2 - h^2}$ $\boxed{z = \hat{z}_0(C_T - 1)}$
Horizontal reflectors (0 or 180 deg.)	$x = 0$ $y = 0$ $z = \hat{z}_0(C_T - 1) + \sqrt{\hat{z}_0^2 {S_T}^2 - h^2}$		$x = 0$ $y = 0$ $z = \hat{z}_0(C_T - 1) - \sqrt{\hat{z}_0^2 {S_T}^2 - h^2}$	
Conditions of existence	$h \leq \hat{z}_0\sqrt{2(C_T - 1)}$ or $T \geq (2/k)\ \cosh^{-1}[(h^2/2\hat{z}_0^2) + 1]$		$k > 0\ ;\ \hat{z}_0\sqrt{2(C_T - 1)} \leq h \leq \hat{z}_0 S_T$ or $(2/k)\ \sinh^{-1}(h/\hat{z}_0) \leq T \leq (2/k)\ \cosh^{-1}[(h^2/2\hat{z}_0^2) + 1]$	

Table 1: Coordinates of some particular points of the constant traveltime surface $F(x, y, z, T) = 0$.
In the above formulas, $\hat{z}_0 = V_0/k$, $C_T = \cosh(kT/2)$, and $S_T = \sinh(kT/2)$.
The framed expressions are independent of the half source-receiver offset h.

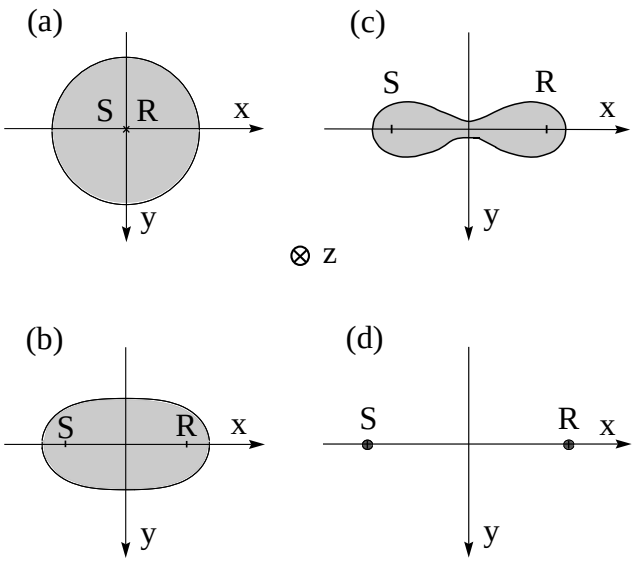

FIG. 3. Trace of the isochron at the surface of the ground ($z = 0$). The parameters used in the calculations are the same as in Figure 2. (a) $h = 0$; (b) $h = 3$; (c) $h = 3.8$; and (d) $h = 5$ km.

The source-receiver offsets considered so far are representative of a conventional near-normal incidence seismic reflection survey. In general, the actual shape of the equal reflection time surface resembles an ellipsoid, but is merely described by a more complicated equation. For greater source-receiver offsets, however, the constant traveltime surface has a radically different shape.

When the distance h is increased from 3 km to 3.8 km (Figures 2c and 3c), the surface folds down to a more compact shape, and its trace in the $z = 0$ plane narrows considerably. In the range 3.8 to 5 km (Figures 2d and 3d), the isochronous surface undergoes rapid and drastic changes. The surface becomes multivalued in x and z inside the subsurface, and takes the form of a tube joining the source and the receiver. In the in-line plane, the upper surface of the isochron corresponds to the secondary branch that has been qualitatively described by Brysk (1990) in the two-dimensional case. The secondary branch emerges at the surface between the source and the receiver, and corresponds to reflections generated from the underside of a reflector.

For very large source-receiver offsets, the constant traveltime problem becomes strongly constrained and the number of possible ray solutions is reduced accordingly. Ultimately, as $h \to \hat{z}_0 \sinh(kT/2)$ (5.3 km with the parameters used in Figures 2 and 3), the thickness of the ray tube shrinks to zero, and the isochronous surface reduces to a line connecting the source S and the receiver R.

There is one more important property of the isochron to be brought out before addressing the MZO application. This property is that Snell's law is satisfied at

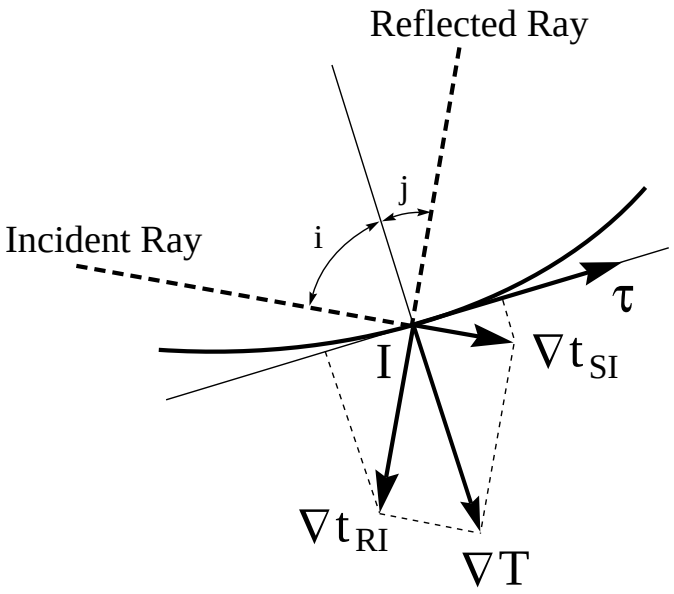

FIG. 4. Verification of Snell's law along the constant traveltime surface.

each reflection point along the isochron. In our formulation of the constant traveltime problem, we did not impose any particular condition on the incidence and reflection angles along the isochronous surface. A confirmation of Snell's law is therefore in order. The demonstration can be carried out in a general manner, for *any* isochronous surface, including those involving a mode conversion at the reflection point. We consider here, for example, an isochronous surface corresponding to a $P-S$ propagation between the source and receiver (Figure 4), and assume that the P- and S-waves propagate in a vertically *and* laterally heterogeneous medium characterized by the velocity distributions $V(\mathbf{x})$ and $W(\mathbf{x})$. Snell's law is then satisfied at point $I(\mathbf{x})$ if

$$\frac{\sin i}{V(\mathbf{x})} = \frac{\sin j}{W(\mathbf{x})} \quad , \tag{13}$$

where i and j are the incidence and reflection angles at point I. This result can be demonstrated by using the constant traveltime condition (2) along with the eikonal equation.

Application of the gradient operator to equation (2) gives

$$\nabla t_{SI} + \nabla t_{RI} = \nabla T \quad , \tag{14}$$

where ∇T is a vector perpendicular to the equal reflection time surface. Consequently, the projection of equation (14) onto a unit vector $\boldsymbol{\tau}$, tangent to the isochronous surface in the plane containing the incident and reflected rays, leads to the relationship

$$\boldsymbol{\tau} \cdot \nabla t_{SI} \; + \; \boldsymbol{\tau} \cdot \nabla t_{RI} \; = \; 0 \quad , \tag{15}$$

which is graphically illustrated in Figure 4. Moreover,

$$|\nabla t_{SI}| = 1/V(\mathbf{x}) \quad ; \quad |\nabla t_{RI}| = 1/W(\mathbf{x}) \tag{16}$$

according to the eikonal equation. We can then write the relations

$$\begin{cases} \sin i \;=\; \cos(\pi/2 - i) \;=\; \dfrac{\boldsymbol{\tau} \cdot \nabla t_{SI}}{|\nabla t_{SI}|} \\ \\ \sin j \;=\; -\;\cos(\pi/2 + j) \;=\; -\;\dfrac{\boldsymbol{\tau} \cdot \nabla t_{RI}}{|\nabla t_{RI}|} \quad , \end{cases} \tag{17}$$

where the right hand side terms can be replaced by their expressions in (15) and (16). The division of these two relations yields equation (13), and completes the demonstration.

Returning to our original problem, it can also be noted that the angle of incidence i relative to the normal to the isochron $F(x, y, , z, T) = 0$ is given by

$$\cos i = \frac{\nabla t_{SI} \cdot \nabla F}{|\nabla t_{SI}||\nabla F|} \quad . \tag{18}$$

Evaluation of the above expression in the crossline direction $x = 0$ yields the remarkably simple result

$$i = \arcsin \left[\frac{h}{\hat{z}_0 \sinh(kT/2)} \right] \tag{19}$$

which shows that the angle of incidence is independent of the reflector dip in the crossline direction.

II. DERIVATION OF THE MZO OPERATOR

With the equation of the constant traveltime surface in hand, we are now able to derive the main characteristics of the normal-incidence ray corresponding to a given reflection point I along the isochron. The combination of all possible normal-incidence rays, for a fixed traveltime T and a given source-receiver separation h, represents the impulse response of the migration to zero offset operator. More precisely, the kinematic part of the MZO operator is a function

$$t_0 = t_0(x_0, y_0) \quad , \tag{20}$$

where t_0 is the two-way traveltime along the normal incidence ray, and (x_0, y_0) are the coordinates of the point of emergence of the ray at the surface of the ground (Figure 5). Similarly, the dynamic part of the MZO operator is a function

$$a_0 = a_0(x_0, y_0) \quad , \tag{21}$$

where a_0 is an amplitude correction to be applied at point (x_0, y_0).

It should be mentioned at this point that the MZO problem has a solution for both the lower and upper surfaces of the isochron. The lower surface represents by far the most important contribution to the MZO operator, because of the very restrictive conditions of existence of the upper surface and because of the considerable energy dispersion associated with that surface. Indeed, it may be noticed that the zero offset rays generated for the upper surface often emerge far outside the source-receiver area, after long traveltimes and with small amplitudes. We will therefore neglect these contributions and restrict our attention to the lower part of the isochron.

The equation of the normal-incidence ray can be found from simple geometrical considerations. The ray M_0I shown in Figure 5 is perpendicular to the isochron at point I, and is contained in a vertical plane P. It follows that the center C of that circular ray can be obtained as the intersection of the vertical tangent to the isochron with the plane $z = -\hat{z}_0$ which contains the centers of all circular rays. The location of the point $M_0(x_0, y_0, 0)$ at the surface of the medium can then be determined by noting that $CI = CM_0 = R_0$, where R_0 is the radius of the circle that supports the ray M_0I.

The analytical solution of the MZO problem is a straightforward application of the preceding remarks. The vertical tangent at the current point $I(x_1, y_1, z_1)$ is colinear to a vector $\boldsymbol{\tau}_2 = \mathbf{n} \wedge \boldsymbol{\tau}_1$, where $\mathbf{n}(F'_{x_1}, F'_{y_1}, F'_{z_1})$ is the direction of the normal at point I, and $\boldsymbol{\tau}_1(-1/F'_{x_1}, 1/F'_{y_1}, 0)$ is the direction of the horizontal tangent at point I. In these expressions,

$$F'_{x_1} = \left.\frac{\partial F}{\partial x}\right|_{x=x_1} \quad , \quad F'_{y_1} = \left.\frac{\partial F}{\partial y}\right|_{y=y_1} \quad \text{and} \quad F'_{z_1} = \left.\frac{\partial F}{\partial z}\right|_{z=z_1}$$

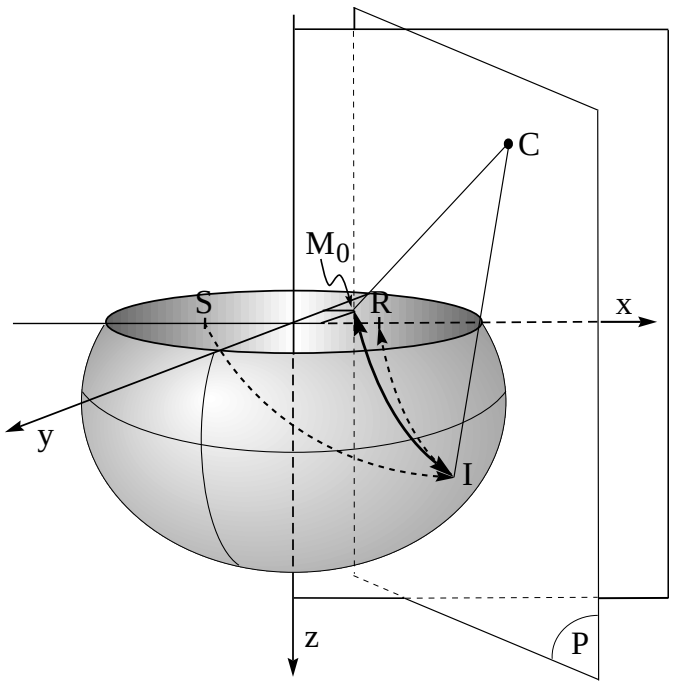

FIG. 5. Construction of the normal incidence ray M_0I for a current point I of the constant traveltime surface. M_0 is the point of emergence of the normal ray at the surface. C is the center of the circle supporting the ray M_0I. M_0, I and C are contained in the vertical plane P.

are the partial derivatives of the constant traveltime surface $F(x, y, z, T) = 0$ at point I. The analytical expressions of these derivatives are easily obtained from equation (9). The equation of the vertical tangent is therefore

$$\frac{x - x_1}{F'_{z_1}/F'_{y_1}} = \frac{y - y_1}{F'_{z_1}/F'_{x_1}} = \frac{-(z - z_1)}{F'_{x_1}/F'_{y_1} + F'_{y_1}/F'_{x_1}} \quad , \tag{22}$$

and the coordinates of the point C are

$$\begin{cases} x_C = x_1 + \hat{z}_1 \dfrac{F'_{x_1} F'_{z_1}}{{F'_{x_1}}^2 + {F'_{y_1}}^2} \\ y_C = y_1 + \hat{z}_1 \dfrac{F'_{y_1} F'_{z_1}}{{F'_{x_1}}^2 + {F'_{y_1}}^2} \\ z_C = -\hat{z}_0 \end{cases} , \tag{23}$$

with $\hat{z}_1 = \hat{z}_0 + z_1$.

The radius R_0 and the ray parameter p_0 of the normal incidence ray are then given by

$$\begin{aligned} {R_0}^2 = 1/(p_0 k)^2 &= (x_C - x_1)^2 + (y_C - y_1)^2 + (z_C - z_1)^2 \\ &= \hat{z}_1^2 \left[1 + \frac{{F'_{z_1}}^2}{{F'_{x_1}}^2 + {F'_{y_1}}^2} \right] \quad , \end{aligned} \tag{24}$$

and the coordinates x_0 and y_0 are solutions of the system

$$\begin{cases} (x_C - x_0)^2 + (y_C - y_0)^2 + {z_C}^2 = {R_0}^2 \\ \\ \dfrac{x_C - x_0}{F'_{x_1}} = \dfrac{y_C - y_0}{F'_{y_1}} \end{cases} \quad . \tag{25}$$

The second equation of the system ensures that M_0 is in the vertical plane P. Solving (25), we find

$$\begin{cases} x_0 = x_1 - \lambda_1 \, F'_{x_1} \\ y_0 = y_1 - \lambda_1 \, F'_{y_1} \end{cases} \quad , \tag{26}$$

where

$$\lambda_1 \;=\; \sqrt{\frac{{R_0}^2 - \hat{z}_0^2}{{F'_{x_1}}^2 + {F'_{y_1}}^2}} \;-\; \frac{\hat{z}_1 \, F'_{z_1}}{{F'_{x_1}}^2 + {F'_{y_1}}^2} \quad .$$

The two-way traveltime t_0 along the ray $M_0 I$ is directly obtained from the traveltime function (A-10) derived in the Appendix

$$t_0 = \frac{2}{k} \; \cosh^{-1} \left[\; \frac{{\xi_1}^2 + \hat{z}_1^2 + \hat{z}_0^2}{2 \; \hat{z}_1 \hat{z}_0} \; \right] \quad , \tag{27}$$

and can be easily calculated since

$${\xi_1}^2 \;=\; (x_1 - x_0)^2 + (y_1 - y_0)^2 \;=\; {\lambda_1}^2 \; ({F'_{x_1}}^2 + {F'_{y_1}}^2) \quad .$$

The fourth parameter characterizing the MZO operator is the amplitude correction a_0. The weighting function a_0 introduced here is based on a geometrical optics approximation to the exact wave theory. It consists of replacing the divergence factor along the SIR raypath by the divergence coefficient corresponding to the $M_0 I M_0$ raypath. The general form of the correction is therefore

$$a_0 = \frac{\mathcal{D}_{M_0 I} \cdot \mathcal{D}_{I M_0}}{\mathcal{D}_{SI} \cdot \mathcal{D}_{IR}} \quad , \tag{28}$$

where

$$\mathcal{D}_{AB} = \sqrt{\frac{\rho_A V_A}{\rho_B V_B}} \;\; \sigma_{AB} \tag{29}$$

denotes the divergence factor between two points A and B. In the latter equation, ρ represents the density of the medium and σ_{AB} is the geometrical spreading of the ray tube connecting A and B. In the case of a linear velocity profile, the geometrical spreading is simply written (see, e.g., Ben-Menahem and Singh, 1981, p. 502)

$$\sigma_{AB} = \frac{\sin i_A}{\xi_{AB}} \quad , \tag{30}$$

where i_A is the take-off angle measured from the vertical at point A, and ξ_{AB}, the horizontal distance travelled between A and B. Consequently, the amplitude correction (28) becomes

$$a_0 = \frac{\sin^2 i_{M_0}}{\sin i_S \sin i_R} \frac{\xi_{SI}\ \xi_{IR}}{\xi^2_{M_0 I}} \quad . \tag{31}$$

The above expression is indeterminate when one of the source, receiver or zero offset rays is vertical. A more convenient expression for a_0 can be obtained by using equation (A-9) in the form

$$\frac{\xi}{\sin i_0} = \hat{z} \sinh kt \quad ,$$

which gives

$$a_0 = \frac{\sinh kt_{SI}\ \ \sinh kt_{IR}}{\sinh^2(kt_0/2)} = \frac{\cosh kT - \cosh k(t_{SI} - t_{IR})}{\cosh kt_0 - 1} \quad . \tag{32}$$

An amplitude correction a_0 greater than 1 means that the cumulative loss of amplitude along the SIR raypath is greater than the loss of amplitude along the normal incidence raypath $M_0 I M_0$. Seismic events characterized by a large value of a_0 are enhanced in the MZO process, whereas arrivals with a small value of a_0 only contribute weakly. Equation (32) also emphasizes the direct relationship between the amplitude a_0 and the traveltimes t_{SI}, t_{IR}, t_0 and T. For nearly horizontal reflectors ($t_{SI} \simeq t_{IR}$) and small velocity gradients k, the correction is approximately given by

$$a_0 \simeq \frac{\cosh kT - 1}{\cosh kt_0 - 1} \simeq \left(\frac{T}{t_0}\right)^2 \quad . \tag{33}$$

The latter expression confirms that the small dips have a predominant effect in the MZO process, since in this case $t_0 < T$. Conversely, it may be noticed that the dips close to 180 degrees corresponding to the upper surface of the isochron (not considered here) are characterized by negligibly small amplitudes because of the large values of t_0. The approximations given in equation (33) are also valid in the crossline direction for all reflector dips.

Finally, since x_0, y_0, t_0 and a_0 can be entirely expressed in terms of the coordinates (x_1, y_1, z_1), the MZO operator can be written in the parametric form

$$\left\{ \begin{array}{rcl} x_0 & = & x_0(\boldsymbol{\eta_1}) \\ y_0 & = & y_0(\boldsymbol{\eta_1}) \\ t_0 & = & t_0(\boldsymbol{\eta_1}) \\ a_0 & = & a_0(\boldsymbol{\eta_1}) \end{array} \right. \quad , \tag{34}$$

where the vector $\boldsymbol{\eta_1}$ describes the constant traveltime surface. In practice, the equation of the isochron is solved for x, y or z, and therefore, x_0, y_0 and t_0 can be parametrized with two variables only: (x_1, y_1), (x_1, z_1), or (y_1, z_1).

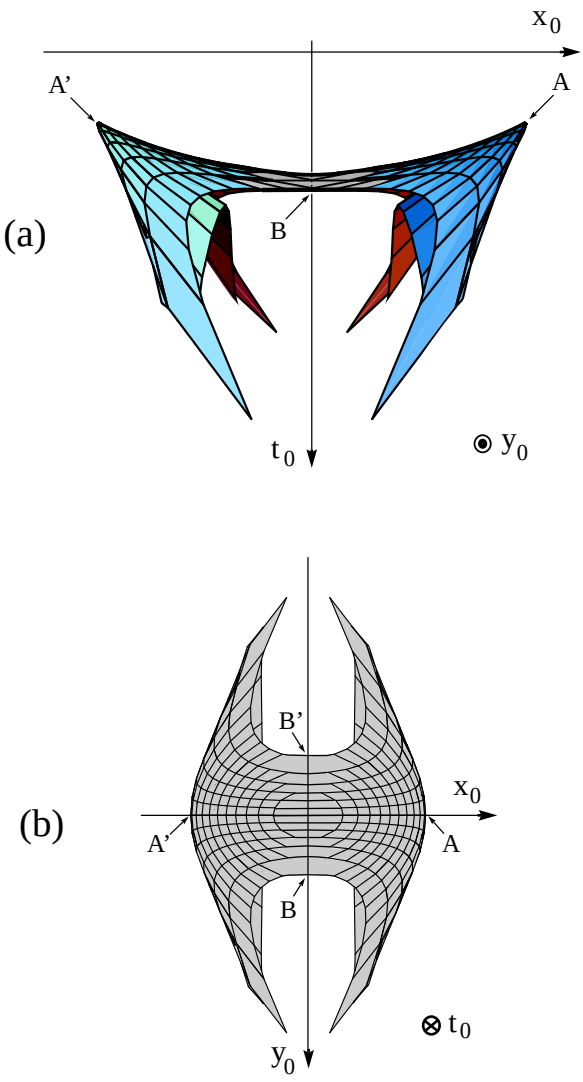

FIG. 6. Cutaway view of the MZO operator in the (x_0, y_0, t_0) space. The parameters used in this figure are $V_0 = 2$ km/s, $k = 1$ /s, $h = 1.5$ km and $T = 2$ s. (a) View from the side (in the y_0 direction); (b) view from above (in the t_0 direction).

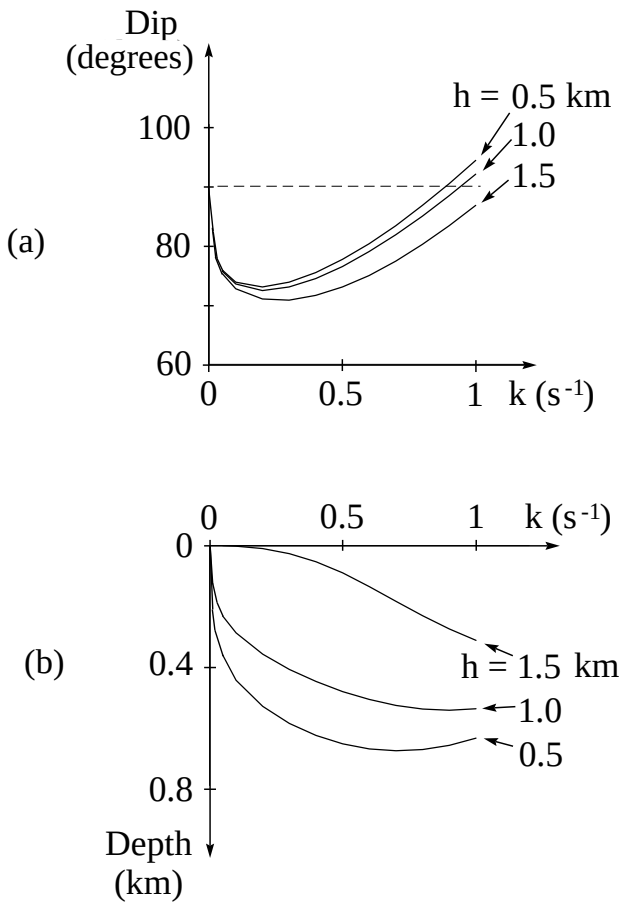

FIG. 7. Characterization of the cusp of the MZO operator in the inline direction. (a) reflector dip at the cusp; (b) reflector depth at the cusp. The curves are plotted as a function of the velocity gradient k for three different values of the half source-receiver offset h with $V_0 = 1.5$ km/s and $T = 2$ s.

Figure 6 is a three-dimensional representation of the kinematic MZO operator in the (x_0, y_0, t_0) space. The two graphs displayed in Figure 6 are incomplete in the y_0 direction to show the full complexity of the MZO impulse response. It is seen that the MZO operator is a multivalued function of x_0, y_0 and t_0 which is characterized by an inner surface and an outer surface. The outer surface represents the small and moderate reflector dips, and corresponds to the "saddle operator" of Perkins and French (1990). In reality, the saddle operator is only a truncated version of the complete MZO operator. The convex inner surface represents additional contributions from steeply dipping or overhanging reflectors. It is usually hidden underneath the exterior surface but can be seen in the cutaway views shown in Figures 6a and 6b.

It is also important to note that the zero-offset correction y_0 given in equation (26) is in fact a negative correction. Therefore, a reflection in the positive y_1 domain is

always mapped into the negative y_0 domain and vice versa. On the other hand, the reflections from the positive x_1 domain are all migrated into the positive x_0 domain (this effect is illustrated in Figure 5). Consequently, the traveltime t_0 for an arbitrary reflection point (x_1, y_1, z_1) is always greater than the traveltime t_0 corresponding to a pure inline ray propagation ($y_1 = 0$), hence the saddle shape of the MZO operator.

The two extremities of the saddle labelled A and A' in Figure 6 mark the transition between the inner and the outer surfaces. The transition is very sharp in the inline direction but becomes more and more gradual as we move away from the x_0 axis. Points A and A' are cusps which are defined by the system of equations

$$\begin{cases} dx_0/dz_1 = 0 & x_0 \text{ maximum} \\ dt_0/dz_1 = 0 & t_0 \text{ minimum} \end{cases} . \tag{35}$$

The above system has no simple analytical solution but can be solved numerically. Figures 7a and 7b respectively show the dip angle and the reflector depth at the cusp as a function of the gradient k for three different source-receiver separations h. In these calculations, $V_0 = 1.5$ km/s and $T = 2$ s are two constant parameters. The curves displayed in Figure 7a show that the cusp corresponds to reflector dips between 70 and 95 degrees in the cases considered. The reflector depth at the cusp is very sensitive to the source-receiver offset and varies between 0 and 700 m (Figure 7b). For instance, when $k = 0.3$ /s and $h = 0.5$ km, the turning point occurs for a reflector at 593 m depth with a dip of 73.7 degrees. This example shows that the inner surface of the MZO operator must be taken into account – at least partially – to image steeply dipping reflectors like salt dome flanks.

The relationship between the MZO operator and the reflector dip is presented in a more general way in Figure 8. This figure shows the two principal cross sections of the MZO operator as a function of the scaled variables x_0/h, y_0/h and t_0/T, and as a function of reflector dip. The parameters used in this calculation are indicated in the figure caption. Figure 8a displays the normal and reverse branches of the MZO operator in the inline direction and shows that the maximum dimensions of this curve are approximately $x_0 \simeq \pm 0.7\ h$ and $t_0 \simeq T$. On the other hand, Figure 8b shows that the hyperbola-shaped curve in the crossline direction is nearly twice as large, with maximum dimensions equal to $y_0 \simeq \pm 1.9\ h$ and $t_0 \simeq 2\ T$. It should also be noticed that the crossline direction $x_0 = 0$ is the only direction in which the MZO operator has no turning point.

Figures 6 and 8 clearly show that the MZO operator is an areal operator which is strongly elongated in the y_0 direction. However, this image is profoundly modified when the reflector dips along the operator are considered. Thus, Figure 8b shows that the relevant contributions in the crossline direction are mostly concentrated near the apex of the hyperbolic curve. It is seen that all dips up to 60 degrees are mapped into a narrow interval between $y_0 = -0.2\ h$ and $y_0 = +0.2\ h$, and that the contributions from steeply dipping reflectors are spread over a very large zone (the

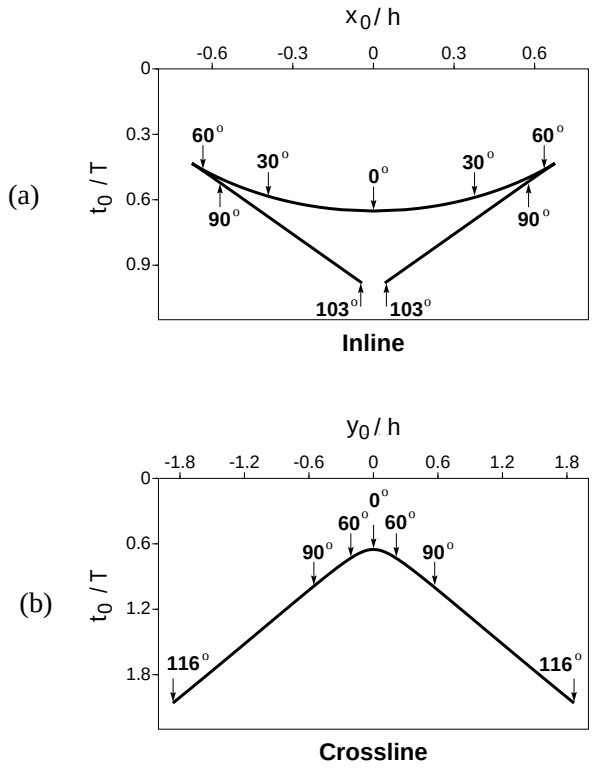

FIG. 8. The MZO operator in the inline (a) and crossline (b) directions as a function of the dimensionless variables x_0/h, y_0/h and t_0/T, and as a function of reflector dip. in this case, $V_0 = 1.5$ km/s, $k = 0.3$ /s, $h = 2$ km and $T = 3$ s.

nearly linear part of the curve). These observations also hold in the inline direction, but to a lesser degree. Figure 8a shows that the reflector dips between 0 and 60 degrees are almost uniformly sampled along the normal branch of the MZO operator. However, the reverse branch exhibits the same stretching as in the orthogonal direction: the long straight segment of the MZO operator mainly corresponds to overhanging reflectors with a maximum dip of 103 degrees.

These results are entirely confirmed by the amplitude curves displayed in Figure 9. The amplitude correction a_0 is computed with equation (32) and is represented by the heights of the shaded areas on top of the traveltime curves. Figure 9a shows that the amplitudes a_0 are almost constant along the normal branch of the MZO operator in the inline direction. Consequently, all dips up to 70 degrees are approximately given the same importance in the MZO processing. Steep dips, on the other hand, contribute only weakly because of their small weighting factors. Indeed, it is seen that the amplitudes taper off along the reverse branch and decrease from 2.5 to 0.3 when the reflector dip increases between 70 and 100 degrees.

The amplitude decay is more dramatic in Figure 9b because of the considerable energy dispersion associated with large dips in the crossline direction. In the

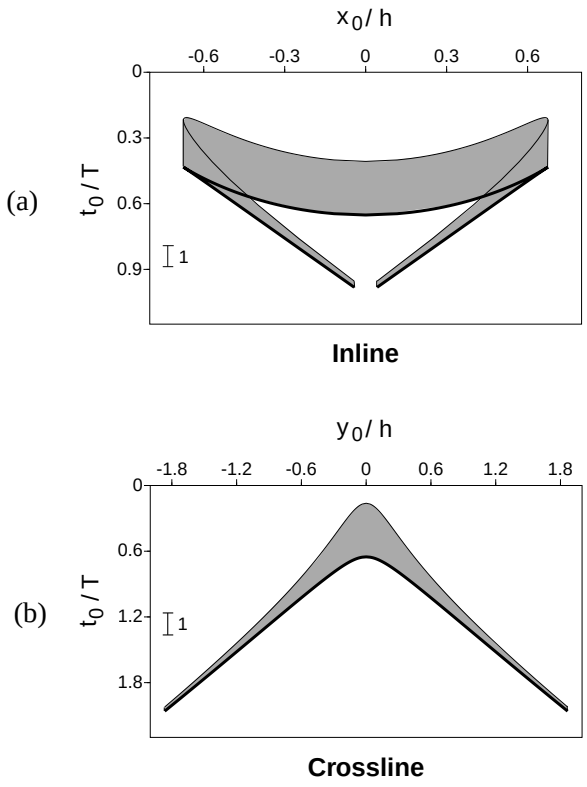

FIG. 9. Divergence correction along the MZO operator in the inline (a) and crossline (b) directions. The height of the shaded areas represents the amplitude correction to be applied along the MZO operator. The parameters used in this figure are the same as in Figure 8.

example considered, the iso-amplitude line at -3 dB crosses the x_0 axis at $x_0 = 0.66\ h$ (beyond the cusp) and the y_0 axis at $y_0 = 0.25\ h$. The -6 dB contour line intersects the x_0 and y_0 axes at $x_0 = 0.59\ h$ and $y_0 = 0.43\ h$ respectively. These values show that the most significant contributions in terms of amplitude are located in a narrow zone along the inline direction. The main consequence of this observation is that the MZO operator can be substantially truncated in the y_0 direction to reduce the computation time of the MZO processing.

The principal characteristics of the MZO operator are listed in Table 2. The properties given in this table include the expressions of the ray parameters p_0 at the edges of the operator, where the dip is maximum. These parameters are crucial in real seismic experiments because they control the minimum trace spacing to use to avoid aliasing effects in the MZO processing. The general expression of the ray parameter p_0 is given by equation (24) and can be written in the classical form

$$p_0 = \frac{\sin \alpha_1}{V(z_1)} \quad , \tag{36}$$

where

$$\alpha_1 = \arctan \sqrt{\frac{F'^{\,2}_{x_1} + F'^{\,2}_{y_1}}{F'^{\,2}_{z_1}}} \tag{37}$$

is the reflector dip at point $I(x_1, y_1, z_1)$.

	Inline Direction	**Crossline Direction**
Reflections	$x_0 = \pm \dfrac{C_T - 1}{S_T} \dfrac{h^2}{\sqrt{2\hat{z}_0^2(C_T+1)+h^2}}$	$x_0 = 0$
at the surface	$y_0 = 0$	$y_0 = \mp \dfrac{h^2}{\sqrt{2\hat{z}_0^2(C_T-1)-h^2}}$
	$t_0 = \dfrac{2}{k}\cosh^{-1}\left[\dfrac{2\hat{z}_0^2 C_T\,(C_T+1)+h^2}{2\hat{z}_0^2(C_T+1)+h^2}\right]$	$t_0 = \dfrac{2}{k}\cosh^{-1}\left[\dfrac{2\hat{z}_0^2 C_T\,(C_T-1)-h^2}{2\hat{z}_0^2(C_T-1)-h^2}\right]$
(Edges / Max. dip)	$p_0 = \dfrac{1}{V_0}\sqrt{\dfrac{2\hat{z}_0^2(C_T+1)+h^2}{\hat{z}_0^2(C_T+1)^2+h^2}}$	$p_0 = \dfrac{1}{V_0}\sqrt{\dfrac{2\hat{z}_0^2(C_T-1)-h^2}{\hat{z}_0^2 S_T^2-h^2}}$
Horizontal	$x_0 = 0$	
reflector	$y_0 = 0$	
	$t_0 = t_n = \dfrac{2}{k}\log\left[\, C_T + \sqrt{S_T^2 - \dfrac{h^2}{\hat{z}_0^2}}\,\right]$	
(Saddle / Zero dip)	$p_0 = 0$	

Table 2: Characteristics of the MZO operator. Same notations as in Table 1. t_n denotes the normal moveout time.

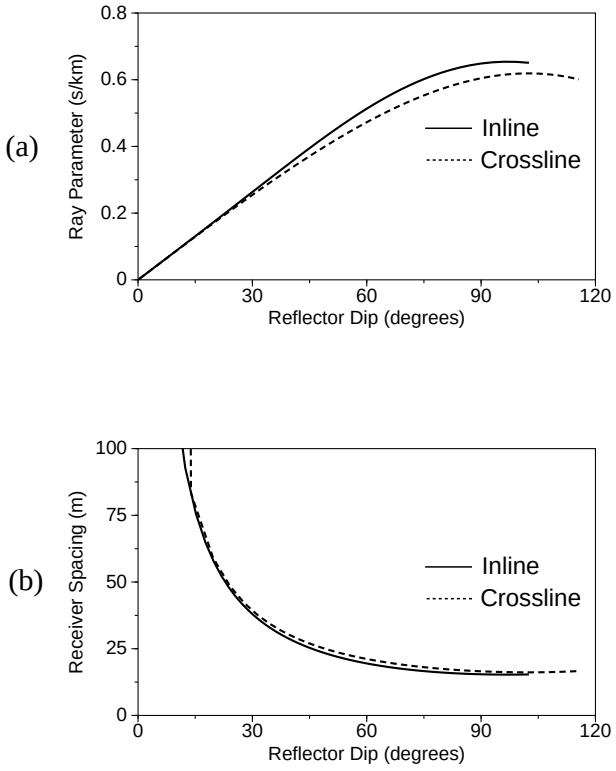

FIG. 10. (a) Graph of the zero offset ray parameter p_0 as a function of reflector dip in the inline and crossline directions. (b) Graph of the corresponding minimum trace spacing for an anti-aliasing protection at 50 Hz. Same parameters as in Figure 8.

Figure 10a displays the variation of the ray parameters $p_0^x = dt_0/dx_0$ and $p_0^y = dt_0/dy_0$ as a function of the reflector dip α_1. It appears that the ray parameters are almost equal in the inline and crossline directions for all reflector dips. The ray parameter p_0^y is slightly smaller than the ray parameter p_0^x because the reflections corresponding to a given dip α_1 occur at a greater depth in the crossline direction than in the inline direction (see, e.g., the vertical reflectors in Figure 2).

The minimum trace spacing Δr required to prevent aliasing effects at a given frequency f is given by

$$\Delta r = \frac{1}{2p_0 f} \tag{38}$$

and is shown in Figure 10b for a reference frequency of 50 Hz. Since the ray parameters p_0^x and p_0^y are nearly identical over the whole range of dips, there are only minor differences between the Δr curves in the inline and crossline directions. As expected, the minimum trace spacing decreases when the dip increases, except for overhanging reflectors where a very slight increase of Δr may be observed. In the example shown, the minimum trace spacing is fairly constant and equal to 15 m for dips greater than 75 degrees. Changing the values of V_0, k, h, T or f modifies

the curvature and the location of the Δr curves but does not modify the fact that the same trace spacing should be used in the inline and crossline directions in actual experiments.

CONCLUSIONS

We have derived an analytical expression for the constant traveltime surface in a depth-dependent medium with a constant velocity gradient. The isochron is given by a quartic equation that can be written in compact form by using the depth variable $\hat{z}$ defined in equation (3). We have also demonstrated that the MZO impulse response is a saddle-shaped operator that is entirely described by our parametric equations (34). These equations allow a fast and accurate determination of the kinematic and dynamic MZO corrections, and should prove useful in areas where a linear velocity gradient is a better approximation than the constant velocity assumption. Besides, the relations and curves presented in this paper are a reference for more complicated background velocity fields.

However, our analysis of MZO processing with constant velocity gradients is not complete. We have shown that the MZO process requires the same trace spacing in the inline and crossline directions to avoid spatial aliasing effects, but we did not propose any practical implementation of the MZO corrections with real data. Furthermore, our amplitude corrections are only valid in the high frequency limit. Ideally, frequency-dependent (wave theoretical) amplitude and phase coefficients should be used to achieve the best results. These issues need to be investigated in detail to demonstrate the superiority of this approach over the conventional MZO processing, when the velocities vary linearly with depth.

ACKNOWLEDGMENTS

We thank Ken Larner for his critical reading of the first draft of this paper, and Paul Docherty for his suggestion to use the eikonal equation to demonstrate that Snell's law is satisfied along any isochronous surface. The authors also thank Alfonso Gonzales for useful discussions on dip moveout processing. This work was completed while M.D. was a visiting scientist at the Center for Wave Phenomena of the Colorado School of Mines. Partial financial support was provided by the Société Nationale Elf Aquitaine. Support was also provided by the the Consortium Project at the Center for Wave Phenomena.

REFERENCES

Artley, C.T., 1991, Dip moveout processing for depth-variable velocity: 61st SEG Annual Meeting, Houston, 10-14 November, Expanded Abstracts, 1204-1207.

Ben-Menahem, A., and Singh, S.J., 1981, Seismic waves and sources, Springer-Verlag.

Brysk, H., 1990, Slotnick revisited: DMO with a linear velocity profile: 60th SEG Annual Meeting, San Francisco, 23-27 September, Expanded Abstracts, 1350-1353.

Deregowski, S. M., and Rocca, F., 1981, Geometrical optics and wave theory of constant offset sections in layered media: Geophys. Prosp. **29**, 384-406.

Hagedoorn, J. G., 1954, A process of seismic reflection interpretation: Geophys. Prosp., **2**, 85-127.

Hale, D., 1984, Dip moveout by Fourier transform: Geophysics, **49**, 741-757.

Hale, D., 1991, A nonaliased integral method for dip moveout: Geophysics, **56**, 795-805.

Meinardus, H.A., and Schleicher, K., 1991, 3-D time-variant dip moveout by the FK method: 61st SEG Annual Meeting, Houston, 10-14 November, Expanded Abstracts, 1208-1210.

Musgrave, A. W., 1961, Wave-front charts and three dimensional migrations: Geophysics, **26**, 738-753.

Notfors, C.D., and Godfrey, R.J., 1987, Dip moveout in the frequency-wavenumber domain: Geophysics, **52**, 1718-1721.

Perkins, W.T., and French, W.S., 1990, 3-D migration to zero offset for a constant velocity gradient: 60th SEG Annual Meeting, San Francisco, 23-27 September, Expanded Abstracts, 1354-1357.

Resnick, J., 1990, Private communication.

Shang, Z., and Starr, E.W., 1991, Three-dimensional velocity-gradient DMO and overhang imaging: 61st SEG Annual Meeting, Houston, 10-14 November, Expanded Abstracts, 1201-1203.

Slotnick, M. M., 1936a, On seismic computations, with applications, I: Geophysics, **1**, 9-22.

Slotnick, M. M., 1936b, On seismic computations, with applications, II: Geophysics, **1**, 299-305.

Slotnick, M. M., 1959, Lessons in Seismic Computing, A Memorial to the Author, SEG Monograph.

Witte, D., 1991, Dip moveout in vertically varying media: 61st SEG Annual Meeting, Houston, 10-14 November, Expanded Abstracts, 1181-1183.

Wolfram, S., 1988, *Mathematica*™, A System for Doing Mathematics by Computer, Addison-Wesley Publishing Company, Inc.

Wunsch, C., 1987, Acoustic tomography by hamiltonian methods including the adiabatic approximation: Reviews of Geophysics, **25**, 41-53.

APPENDIX:
EXPRESSION OF THE TIME-DISTANCE FUNCTION

In the vertically heterogeneous medium described by equation (1), the ray starting at the origin O with take-off angles i_0 relative to the z-axis, and ϕ_0 relative to the x axis, propagates in a vertical plane and can be described by a circle centered at

$$\left\{ \begin{array}{l} x_c = \hat{z}_0 \ \cot i_0 \ \cos\phi_0 \\ y_c = \hat{z}_0 \ \cot i_0 \ \sin\phi_0 \\ z_c = -\hat{z}_0 \end{array} \right. \quad , \tag{A-1}$$

with a radius $\rho = \left| \dfrac{\hat{z}_0}{\sin i_0} \right|$. Its equation can be written in the form

$$[\ \xi - \hat{z}_0 \cot i_0\ ]^2 \ + \ [\ z + \hat{z}_0\ ]^2 \ = \ \hat{z}_0^2 (1 + \cot^2 i_0) \quad , \tag{A-2}$$

where $\xi = \sqrt{x^2 + y^2}$ is the horizontal distance travelled along the ray.

The ray propagation can be further described by the traveltime $t = t(p,z)$ and distance $\xi = \xi(p,z)$ functions. The total traveltime t from the surface to depth z for a given ray parameter

$$p = \frac{\sin i(z)}{V(z)} = \frac{\sin i_0}{V_0} \tag{A-3}$$

can be computed by integrating the elementary traveltimes along the raypath:

$$t(p,z) \ = \ \int_0^z \frac{dz}{V(z)\sqrt{1 - p^2 V(z)^2}} \ = \ \frac{1}{k} \left[\ \cosh^{-1} \frac{1}{pV_0} + \varepsilon \cosh^{-1} \frac{1}{pV(z)} \ \right] \quad , \tag{A-4}$$

where

$$\varepsilon = \left\{ \begin{array}{rl} -1 & \text{before the turning point,} \\ 0 & \text{at the turning point [} p = 1/V(z) \text{],} \\ +1 & \text{beyond the turning point.} \end{array} \right.$$

Similarly, the horizontal distance ξ travelled along the ray to depth z can be expressed as

$$\xi(p,z) \ = \ \int_0^z \frac{p \ V(z) \ dz}{\sqrt{1 - p^2 V(z)^2}} \ = \ \frac{1}{pk} \left[\ \sqrt{1 - p^2 {V_0}^2} + \varepsilon \sqrt{1 - p^2 V(z)^2} \ \right] \quad . \tag{A-5}$$

The ambiguity related to the presence (or not) of a turning point along the ray can be removed by writing t as a function of ξ.

Using the addition rule $\cosh^{-1} a \ \pm \ \cosh^{-1} b = \cosh^{-1}[\ ab \ \pm \ \sqrt{(a^2-1)(b^2-1)}\ ]$, equation (A-4) can be alternatively written in the form

$$t(p,z) = \frac{1}{k} \cosh^{-1} \left\{ \frac{1}{p^2 V_0 V(z)} \left[\ 1 + \varepsilon \sqrt{(1 - p^2 {V_0}^2)(1 - p^2 V(z)^2)} \ \right] \right\} \quad . \tag{A-6}$$

Then, using the relation $\sinh^2 a = \cosh^2 a - 1$, we obtain

$$\sinh^2 kt = \frac{k^2 \xi^2}{p^2 {V_0}^2 V(z)^2} \quad ,$$

or equivalently,

$$t(\xi, z) = \frac{1}{k} \sinh^{-1} \left[\frac{k\ \xi}{p V_0 V(z)} \right] \quad . \tag{A-7}$$

The next step consists of eliminating the ray parameter p appearing in equation (A-7) to obtain an expression which depends only on the space variables ξ and z, and on the parameters V_0 and k (i.e., $\hat{z}_0$). This can be done by solving equation (A-2) for $\cot i_0$

$$\cot i_0 \ = \ \frac{\xi^2 + z^2 + 2z\hat{z}_0}{2\ \xi \hat{z}_0} \ = \ \frac{\xi^2 + \hat{z}^2 - \hat{z}_0^2}{2\ \xi \hat{z}_0} \quad . \tag{A-8}$$

Therefore, by writing (A-7) in the form

$$t(\xi, z) \ = \ \frac{1}{k} \sinh^{-1} \left[\frac{\xi}{\hat{z} \sin i_0} \right] \ = \ \frac{1}{k} \sinh^{-1} \left[\frac{\xi}{\hat{z}} \sqrt{1 + \cot^2 i_0} \right] \quad , \tag{A-9}$$

we find

$$t(\xi, z) = \frac{1}{k} \sinh^{-1} \sqrt{\left[\frac{\xi^2 + \hat{z}^2 + \hat{z}_0^2}{2\ \hat{z}\hat{z}_0} \right]^2 - 1} \quad , \tag{A-10}$$

that is,

$$t(\xi, z) = \frac{1}{k} \cosh^{-1} \left[\frac{\xi^2 + \hat{z}^2 + \hat{z}_0^2}{2\ \hat{z}\hat{z}_0} \right] \quad . \tag{A-11}$$

Equation (A-10) is a generalization of the well-known time-distance curve $t(\xi) = (2/k) \sinh^{-1}(\xi / 2\hat{z}_0)$ which is valid at the surface of medium with a linear velocity gradient (see, e.g., Slotnick, 1959, p. 215). The time-distance function (A-10) can be used to analyze or compute traveltimes for a buried source or receiver, provided that the velocity distribution under consideration is adequately represented by a linear gradient.

FIGURE CAPTIONS

Figure 1: The constant traveltime problem between a fixed source S, a reflection point I, and a fixed receiver R.

Figure 2: Graphical representation of the constant traveltime surface for a fixed traveltime T, and for four different values of the half source-receiver offset h. The contour levels represent the y dimension of the surface. In this example, $V_0 = 2$ km/s, $k = 1$ /s, and $T = 3.4$ s. (a) $h = 0$; (b) $h = 3$; (c) $h = 3.8$; and (d) $h = 5$ km.

Figure 3: Trace of the isochron at the surface of the ground ($z = 0$). The parameters used in the calculations are the same as in Figure 2. (a) $h = 0$; (b) $h = 3$; (c) $h = 3.8$; and (d) $h = 5$ km.

Figure 4: Verification of Snell's law along the constant traveltime surface.

Figure 5: Construction of the normal incidence ray M_0I for a current point I of the constant traveltime surface. M_0 is the point of emergence of the normal ray at the surface. C is the center of the circle supporting the ray M_0I. M_0, I and C are contained in the vertical plane P.

Figure 6: Cutaway view of the MZO operator in the (x_0, y_0, t_0) space. The parameters used in this figure are $V_0 = 2$ km/s, $k = 1$ /s, $h = 1.5$ km and $T = 2$ s. (a) View from the side (in the y_0 direction); (b) view from above (in the t_0 direction).

Figure 7: Characterization of the cusp of the MZO operator in the inline direction. (a) reflector dip at the cusp; (b) reflector depth at the cusp. The curves are plotted as a function of the velocity gradient k for three different values of the half source-receiver offset h with $V_0 = 1.5$ km/s and $T = 2$ s.

Figure 8: The MZO operator in the inline (a) and crossline (b) directions as a function of the dimensionless variables x_0/h, y_0/h and t_0/T, and as a function of reflector dip. In this case, $V_0 = 1.5$ km/s, $k = 0.3$ /s, $h = 2$ km and $T = 3$ s.

Figure 9: Divergence correction along the MZO operator in the inline (a) and crossline (b) directions. The height of the shaded areas represents the amplitude correction to be applied along the MZO operator. The parameters used in this figure are the same as in Figure 8.

Figure 10: (a) Graph of the zero offset ray parameter p_0 as a function of reflector dip in the inline and crossline directions. (b) Graph of the corresponding minimum trace spacing for an anti-aliasing protection at 50 Hz. Same parameters as in Figure 8.